Materials Today Communications 35 (2023) 106127

Contents lists available at ScienceDirect

Materials Today Communications

journal homepage: www.elsevier.com/locate/mtcomm

Automated image segmentation of scanning electron microscopy images of graphene using U-Net Neural Network

Aagam Shah [a], Joshua A. Schiller [b], Isiah Ramos [a], James Serrano [c], Darren K. Adams [d], Sameh Tawfick [b], Elif Ertekin [b,e,*]

[a] Department of Materials Science & Engineering, 1304 W Green Street, University of Illinois at Urbana-Champaign, Urbana IL 61801, United States of America
[b] Department of Mechanical Science & Engineering, 1206 W Green Street, University of Illinois at Urbana-Champaign, Urbana IL 61801, United States of America
[c] Department of Computer Science, 4400 University Drive MSN 4A5, George Mason University, Fairfax VA 22030, United States of America
[d] National Center for Supercomputing Applications, University of Illinois at Urbana-Champaign, Urbana IL 61801, United States of America
[e] Materials Research Laboratory, University of Illinois at Urbana-Champaign, Urbana IL 61801, United States of America

ARTICLE INFO

Dataset link: https://github.com/nanoMFG/unet-sem

Keywords:
Graphene
Scanning electron microscopy
Machine learning
Chemical vapor deposition

ABSTRACT

Scanning electron microscopy (SEM) is one of the most common approaches to the characterization of synthesized 2D materials such as graphene. Images from SEM contain detailed information about crystalline properties, domain size, and nucleation density, but typically are analyzed through a laborious, serial process that relies on the trained eye of synthesis experts. In this work, we demonstrate an image segmentation neural network that automatically distinguishes between pixels in SEM images that correspond to regions where graphene is and is not present. We utilize the U-Net architecture to learn on a training data set of more than 90 pre-labeled images coupled with moderate image augmentation. Comparing the performance of models trained on smaller high fidelity data set to those trained on larger low fidelity data sets, we find that higher quality is more valuable than higher quantity for achieving good performance. When neural network hyperparameters such as batch size and learning rate are properly tuned, the learned model shows an accuracy for classification of over 90% and an F1 score over 80%. The neural network trained on SEM images of graphene shows reasonable performance when directly applied to other 2D materials, suggesting the possibility of use in transfer learning. Detailed analysis of the inner workings of the model reveals that the domain edges are most critical for making classifications when segmenting the image. We also show the use of a post processing technique to estimate the graphene domain size using segmented masks. This demonstration shows the potential for SEM image segmentation at scale using deep learning approaches and gives insights into best practices for improving model performance.

1. Introduction

Rapid, efficient, and accurate characterization of graphene will accelerate the discovery of scalable manufacturing recipes to enable high performance mechanical [1,2] and electrical devices [3–6]. After years of effort, synthesis still remain a pervasive challenge [7–10]. Scalable manufacturing of graphene-based electronics requires high quality graphene synthesized reliably on substrates compatible for device use. Currently, synthesis recipes suffer from trade-offs between repeatability, quality, and growth conditions [11]. For instance, high quality graphene with large single crystalline orientation requires expensive single crystalline catalyst substrates, extremely demanding conditions (temperature and duration), or inefficient transfer from growth to device substrate [11].

An elusive bottleneck to explore and optimize synthesis recipes is the slow, qualitative, and laborious process of characterizing the produced graphene. Most commonly, scanning electron microscopy (SEM) images are used to analyze samples and collect quantitative data [12]. SEM images provide information such as coverage (percentage of the area covered by graphene), domain (or grain) size and shape, and nucleation density — important metrics to quantify the quality of synthesized material. But producing these metrics efficiently requires accurate, automated methods of feature extraction that overcome the time intensive analysis process. Feature extraction from SEM images of 2D materials at scale could be used by data-driven or machine learning techniques in a closed loop optimization of synthesis recipes towards reliable manufacture of large quantities of graphene.

* Corresponding author at: Department of Mechanical Science & Engineering, 1206 W Green Street, University of Illinois at Urbana-Champaign, Urbana IL 61801, United States of America.
E-mail address: ertekin@illinois.edu (E. Ertekin).

https://doi.org/10.1016/j.mtcomm.2023.106127
Received 22 February 2023; Received in revised form 20 April 2023; Accepted 3 May 2023
Available online 9 May 2023

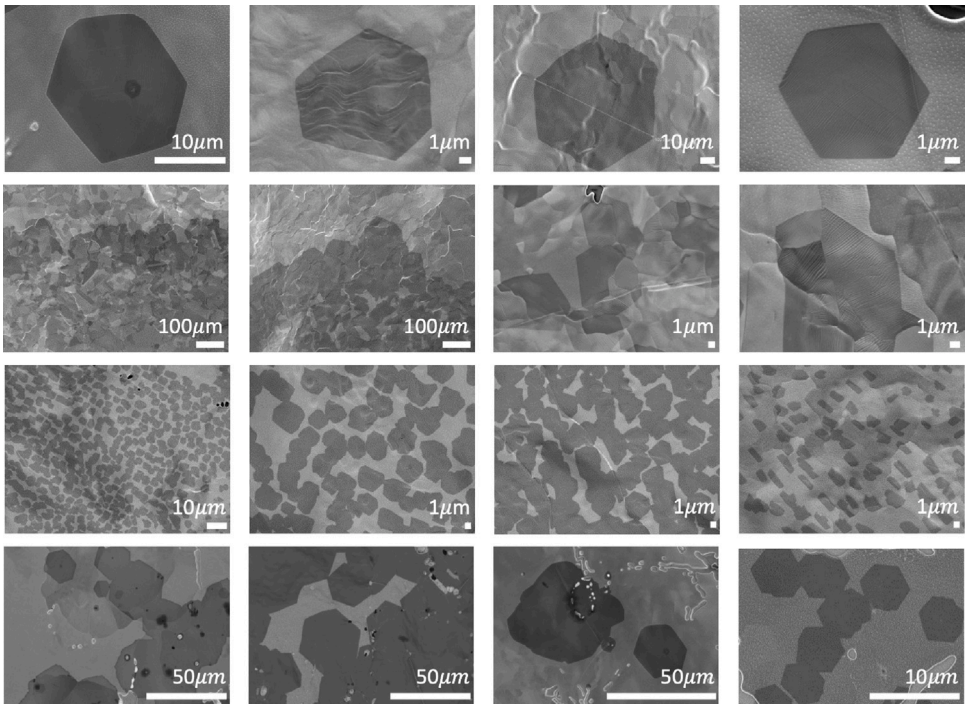

Fig. 1. Example SEM micrographs of graphene showing a diversity of coverage, contrast, flake size, and flake shape in the graphene domains taken at varying magnifications. Some images contain artifacts which makes the task of segmentation more difficult.

In the past few years, several machine and deep learning techniques have been employed for segmentation of microscopy images with both speed and accuracy. While most of these techniques have been applied to optical images [13–22], a few have focused on transmission [23–31] or scanning [32,33] electron microscopy. Optical microscopy often generates colorful images with sharp features and contrast. Machine and deep learning approaches here largely employ supervised learning [13–16,20–22,27–31], although a few unsupervised methods also work well [17–19]. The contrast and distinctive features offered by optical micrographs of 2D materials have enabled real-time detection within autonomous robotic systems [14], detection of diverse materials and van der Waals heterostructures [15], and feature analysis including edges, shapes, flake sizes, and their distributions [13]. Analysis of electron microscopy images has proven to be more challenging. Whereas optical microscopy provides red–green–blue (RGB) channels for data analysis, the gray scale nature of electron microscopy images inherently contains less information (a single channel) to distinguish features. Applications of deep learning to electron microscopy images include nanoparticles and their coarsening dynamics [23,31], neuronal membranes [24], defect detection [27–30], and classification of disparate types of 0D, 1D, 2D, and 3D nanostructures [32,33]. For electron microscopy images, most techniques to date use neural networks [23,24,32] with architectures such as AlexNet, ResNet, and U-Net. AlexNet [34] is the first study using convolutional neural networks (CNNs) in the field of computer vision and is still widely used. The "levels" of features identified by such networks can be improved by increasing the number of layers (depth) in such networks. Unfortunately, a result of increasing depth is often higher training and testing error [35]. ResNet [35] is another popular CNN architecture employed for computer vision tasks. It uses "shortcut connections" to allow the network to skip a few layers and tackle the problem of rising error. Both these architectures require large training data sets, ranging from 500 to millions of training images, which is not ideal for applications involving 2D materials where a labeled data set of images does not exist. U-Net [36], an encoder–decoder that can be trained on relatively small data sets, stands out for its effectiveness in the medical field [37–41] and on optical images of 2D materials [13–16,20–22].

Segmentation of SEM images of 2D materials like graphene presents unique hurdles for deep learning approaches. Graphene, when viewed in an SEM, exhibits a visual contrast from its surroundings that makes it amenable for automated image segmentation [12]. Yet, graphene shows up in various sizes and shapes (although ideally hexagonal), various contrast ratios, and often with many artifacts and other undesirable features present (see Fig. 1). Due to graphene's 2D nature, images do not benefit from distinctive differences in dimensionality and depth. Due to this complexity, simple techniques such as binary color masking are inaccurate (see example in Figure S1). Unsupervised techniques such as *k*-means clustering [42] are not scalable, since they require time-consuming manual input from users to select the number of clusters, adjust hyperparameters, and assign labels to each cluster (Figure S2). Neural network based approaches that work with gray scale electron microscopy images have been developed for, e.g., nanoparticles with depth [32,33] or cross sections of 3D materials with regular defining features [23,24]. However, their application to 2D materials is challenging since these models may have difficulty extracting meaningful features from images that lack depth and exhibit irregularity in shape, contrast, and size.

In this work, we demonstrate the application of U-Net to automated segmentation of SEM images of graphene synthesized by chemical vapor deposition (CVD). We use software developed in-house, as part of the Graphene Recipes for Synthesis of high Quality materials (GrResQ) framework [43], to first generate a data set of training images. Using this data set, we train a U-Net neural network to segment SEM images of graphene into pixels that contain and pixels that do not contain graphene, and show that it can automatically and rapidly quantify the coverage of graphene. We analyze the effect of training data quality on the performance of the model, and find that a smaller set of high quality training data is more valuable than a larger set of lower quality training data. The model trained on images of graphene is additionally able to segment SEM images of other 2D materials with reasonable accuracy, showing promise for transfer learning. Since

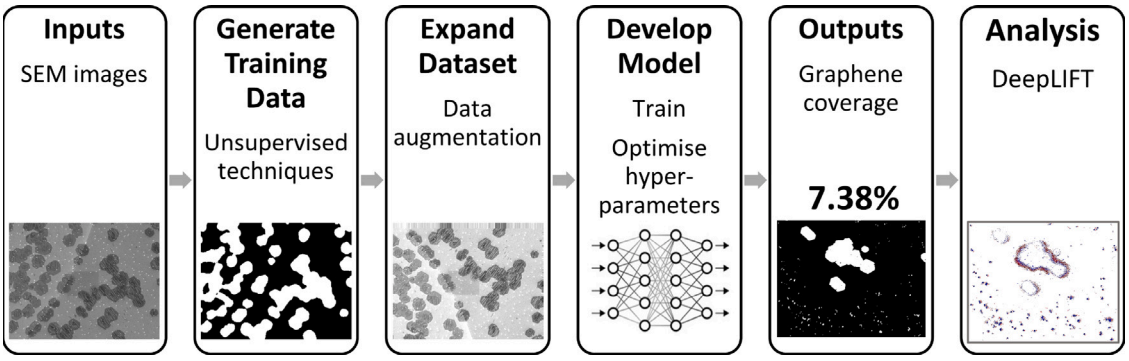

Fig. 2. Workflow for the training of a neural network to automate the analysis of SEM images of graphene. First SEM images of graphene samples are segmented using unsupervised techniques to generate training data. Data augmentation is sued to generate a larger data set of training images. Then the U-Net neural network is trained and its hyperparameters optimized. The trained model is capable of calculating the percent coverage of graphene. Finally, the trained model is analyzed to obtain a better understanding of the inner workings of the neural network.

Table 1
Parameters used for image augmentation.

Operation	Range
Rotation	±20°
Width Shift	5%
Height Shift	5%
Shear	0.05 radians
Zoom	95–105%
Brightness	$\gamma = [0.2, 1.8]$
Vertical Flip	50%
Horizontal Flip	50%

neural networks are sometimes viewed as "black box" methods, we perform DeepLIFT [44] analysis to obtain a visual interpretation of the inner workings of the model, which provides insights into the key aspects of the image that enable accurate classification. This work presents an automated technique for the analysis of SEM images of graphene, towards fostering the closed loop optimization of synthesis recipes for scalable manufacturing. The trained model is available for general use [45], and is compatible with deepImageJ [46], a plug-in that allows users to use pre-trained neural networks in ImageJ and Fiji.

2. Methods

Fig. 2 shows the complete workflow we used. To generate training data for the neural network, starting with a set of SEM images we first created a binary mask for each image that segments the image into regions that contain graphene and those that do not. For this, we used techniques such as template matching [47] and k-means clustering [42] for accelerated mask generation with the help of the Gr-ResQ Image Tool [48]. We next applied data augmentation to grow the data set, used the masks to train a U-Net neural network, and explored different batch sizes and learning rates to find the optimal hyperparameters. Once a good model was obtained, we performed DeepLIFT analysis to identify the importance of each pixel in the segmentation process to get insights into how the neural network determinations are made. These steps are discussed in more detail below.

2.1. Generation of training data

To begin, we collected a comprehensive set of 203 SEM images from in-house CVD graphene synthesis experiments that were carried out over the last ~5 years in the Kinetic Materials Research Group (lead: Tawfick). These images were collected under diverse conditions using several different scanning electron microscopes. A selection of these images is presented in Fig. 1, showing a diversity of nucleation densities, flakes sizes and shapes, and different magnifications. Some images show large monodomain regions, while others show large numbers of small hexagons distributed across the field of view. Some images may not even contain discernable graphene.

Using this collection of images, we generated 113 "high fidelity" masks, which were split into 93 training and 20 testing high fidelity masks, and 90 "low fidelity" masks (all subsequently used for training). While high fidelity masks are those could be accurately segmented using manual techniques, the low fidelity set comprises images with complex features that made manual mask generation challenging and resulted in less accurate masks. Examples include images with large numbers of small, disperse graphene domains spread across the SEM field or images that include artifacts or contaminants that were difficult to distinguish from substrate or graphene. Masks from such images proved to be too cumbersome or even impossible to fix manually. Note that the distinction between high and low fidelity was made by human inspection, and a selection of examples of high and low fidelity masks are shown in the Supporting Information (Figure S3).

Due to the laborious process creating masks manually to use for training data, our set of training images is small in comparison to some other data sets used for segmentation of images from electron microscopy. For example, the general purpose shared data set [49] used in Refs. [32,33] contains ~18,580 images from a variety of sources including biological systems, fibers, MEMS devices, patterned surfaces, and others but does not contain images of 2D materials that are of interest here. A data set of 2,400 TEM images was generated to train a neural network to detect nanoparticles on a substrate [23]. On the other hand, only 30 images were used to train a neural network for the specific application of identification of neuronal membranes from TEM images [24], showing that segmentation is possible on smaller data sets for dedicated applications.

To capitalize on the relatively small data set of images, we employed data augmentation to generate and provide images of varying shape, size, contrast, and other sources of complexity of SEM images of graphene. For each augmented batch, an image was selected and the following augmentations were performed: rotation, shift, shearing, magnification, horizontal and vertical flipping, and brightness modification. The parameters for these augmentations are summarized in Table 1. These augmentations were applied to both the high and low fidelity data sets.

2.2. U-Net neural network

U-Net is a convolutional neural network (CNN) architecture that reduces an input image to a latent space representation with successive downsampling. This latent representation is then upsampled with each layer including additional input from the downsampling steps to impart contextual information to the output. To create the neural network, we used the Keras/Tensorflow python framework [50,51] run in parallel across 8 Volta100 GPUs.

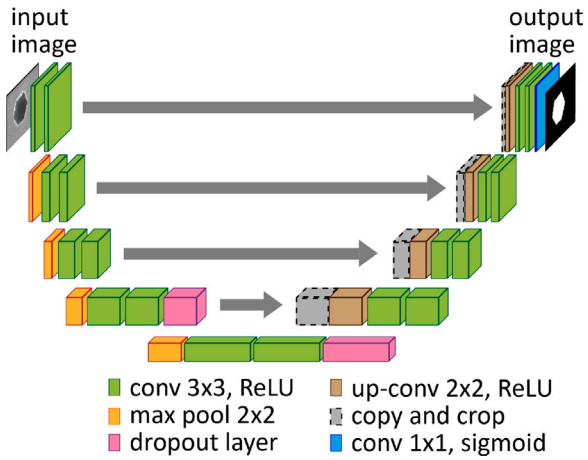

Fig. 3. The U-Net architecture. The encoding half of the U-Net reduces the input to a latent space representation where the relevant pixels are activated and the decoding half brings the latent space representation back to 2D space with the copy and crop steps imparting contextual and spacial information. Legend: ReLU denotes Rectified Linear Unit (ReLU) activation; the dropout layer uses a 0.5 dropout rate; "copy and crop" indicates a concatenation layer with information copied and cropped from a previous layer.

The specific architecture we used is illustrated in Fig. 3. The 512 × 512 resolution input image is first run through two convolution layers (with padding) with 3 × 3 tile sizes. The output is then put through a 2 × 2 max pooling layer. This process is repeated three more times, with the last downsampling iteration adding a 50% dropout step before max pooling. The first convolution increases the number of channels to 64 and for each subsequent level, the number of channels is doubled until there are 1024 channels as illustrated. The first upsampling step is also combined with a 50% dropout layer. Each upsampling step goes through a 3 × 3 convolution layer that halves the number of channels. It is then concatenated with the output from the convolution layer from a corresponding downsampling step, as indicated by the gray arrows in Fig. 3. Following two more convolution layers, the number of channels is halved. The upsampling step is repeated three more times until the number of channels is again 64. The output is then fed into one last 3 × 3 convolution layer with two input channels and a 1 × 1 convolution layer with a single output channel. With the exception of the last layer which has a sigmoidal activation, all activations are rectified linear unit (ReLU) functions. The model was trained with batch sizes of 8, 16, and 32 images for 100 epochs. We used the binary cross entropy to calculate the loss as:

$$L(x, z) = -(z \log(g(x)) + (1 - z) \log(1 - g(x))) \quad (1)$$

where x are the logits (converted from the output layer), z are the labels (i.e. 0 or 1), and g is the sigmoid function. To calculate the gradient updates, we used the RMSprop optimizer with an initial learning rate of 0.0001.

2.3. Domain size estimation via post-processing

As the trained network outputs pixel masks with classification of graphene vs. background, post-processing of these masks is needed for analysis of other quantities of interest such as domain size or regularity of crystalline domains. As an example of post-processing images for structural analysis, we have developed an automated technique to automatically calculate the mean domain size of the graphene domains in the image from the model output, i.e. the binary segmented images. In this subsection, "domain" indicates a single grain of graphene, and "continent" indicates an area of continuous connected domains. Fig. 4 shows the steps in this technique for an example image. To estimate domain size, the image is first divided into individual continents. All continents with an area exceeding 0.4% of the image area are then included for subsequent analysis, with the others ignored. For each continent, Canny edge detection [52] is used to detect edges, and probabilistic Hough transform [53] is used to return small line segments along the edges of the continents. These small line segments are then joined to form larger line segments based on their proximity in distance and orientation. Then, starting at a randomly picked corner of a segment, these long line segments are connected as linked lists of vectors, where each linked list contains only the segments connected to each other in a convex loop. Each convex loop indicates a separate domain along the edge of a continent. For each convex loop, the end is connected to the beginning and the enclosed area is measured.

Table 2
Multiplication factor used in domain size calculation. The angle indicates the angle between the first and last vector of the convex loop signifying the edge of a domain, measured in radians.

Angle (θ)	Multiplier
$\theta < \frac{\pi}{6}$	0
$\frac{\pi}{6} < \theta < \frac{2\pi}{6}$	10.0
$\frac{2\pi}{6} < \theta < \frac{3\pi}{6}$	6.0
$\frac{3\pi}{6} < \theta < \frac{4\pi}{6}$	4.0
$\frac{4\pi}{6} < \theta < \frac{5\pi}{6}$	3.0
$\frac{5\pi}{6} < \theta < \frac{6\pi}{6}$	2.0
$\frac{6\pi}{6} < \theta < \frac{7\pi}{6}$	1.2
$\frac{7\pi}{6} < \theta$	1.0

Since the domain might be only partially visible in the SEM field of view, a multiplication factor is needed to estimate the true area of the domain. This factor is calculated from Table 2 based on the angle between the first and last vectors of the convex loop. The final estimated area of the continent is given by the product of this multiplication factor with the measured area of the continent. The mean domain area and number of domains in each continent are obtained by assuming that the mean area of all domains in the continent is the same as the mean area of all domains along the edge of that continent. To estimate the mean domain area across all the continents in one image, the total area of all continents analyzed is divided by the total number of domains. Finally, the mean domain size is estimated, assuming ideal regular hexagons for each domain.

The results from this method were compared with manually analyzed images and showed agreement for most cases. The most common source of error arises in cases where the total area covered comes from a large number of small continents, each <0.4% of the total area and therefore ignored. Such images have a very small mean domain size, but some continents are very large because many domains overlap each other. To mitigate this source of error, the area of all continents is plotted in ascending order and the elbow point of the curve is picked as a cutoff, to ignore continents with large number of connected domains. The mean area of the remainder of the continents is used as a measure of the mean area of the domains in the image and the mean domain size is calculated as described above. The results from this method were also compared with manually analyzed images and found to be in agreement.

3. Results and discussion

3.1. Effect of quality of data set

A critical consideration when using ML models for image segmentation is the quality of the training data. Since preparing training data is a laborious process, understanding the trade off between data

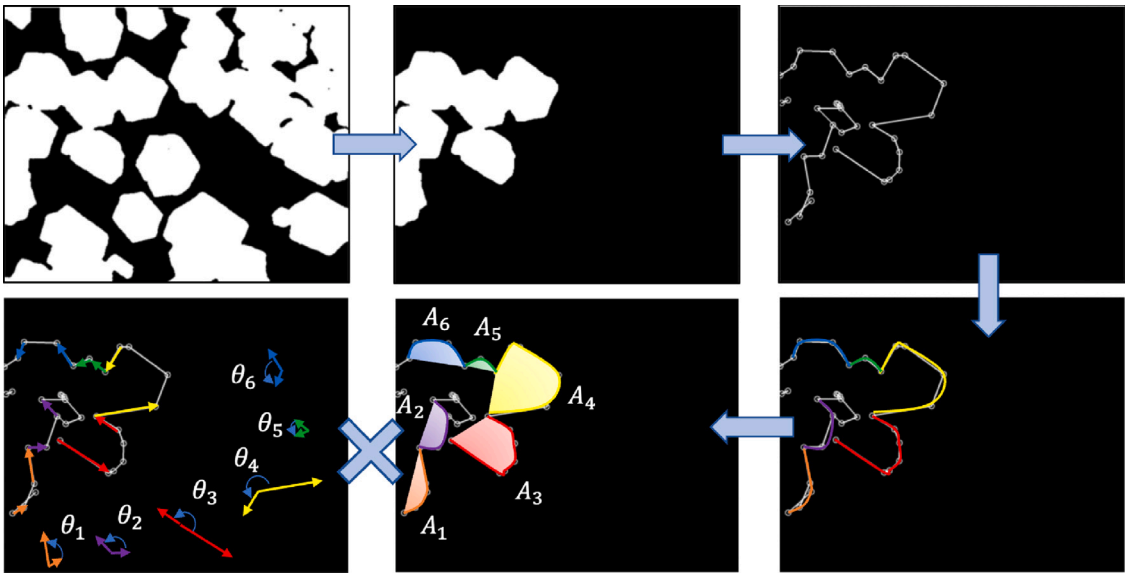

Fig. 4. Approach to estimating domain size from a segmented mask: (i) the image is divided into individual "continents" each having multiple merged graphene domains, and (ii) canny edge detection and probabilistic Hough transform are used to identify small line segments along the edges of each continent. (iii) Line segments are joined based on their proximity in distance and orientation to form larger line segments, and (iv) the larger segments are then grouped into convex loops, and stored as a linked list. Each convex loop represents one domain. (v) For each convex loop, the area covered (A_i) and angle between the first and last vector of the linked list (θ_i) is measured. (vi) The angle is used to determine a multiplication factor, whose product with the measured area is equal to the calculated area of each domain in that continent.

set quantity and quality can help to most efficiently create useful data sets that train effective models. We therefore began by assessing the performance of U-Net on two sets of masks: (i) accurate masks generated from 93 high-fidelity images (called "high-fidelity"), and (ii) a set of masks generated from the "high fidelity" and "low fidelity" data set combined (labeled "all"). Data augmentation was included for both cases. While the high fidelity data set contained more accurate training images, it was only approximately half as large as the "all" data set.

Figs. 5(a, b) show the accuracy and the loss during training. The model trained on the "high fidelity" data set is represented by the red curves and the model trained on the "all" data set is represented by the blue curves. For both cases, the light-colored curves represent the training loss and accuracy, and the dark curves represent the test loss and accuracy. These models were trained with a batch size of 16 and a learning rate of 10^{-4}. When trained on the high fidelity data set, the training and test accuracy were similar. By contrast, when trained on "all", the difference between the training and test loss was observed to increase with epoch.

This observation is indicative of a substantial difference in training data (sometimes called a *data set shift*) between the two data sets. The neural network trained on "all", as a result of having trained on less accurate data, was unable perform as well as the neural network trained on only the high-fidelity training data, when assessed on the same testing set. This evaluation indicates that, for use cases like ours, higher quality data sets even if smaller may be better for training than larger data sets containing less accurate training information.

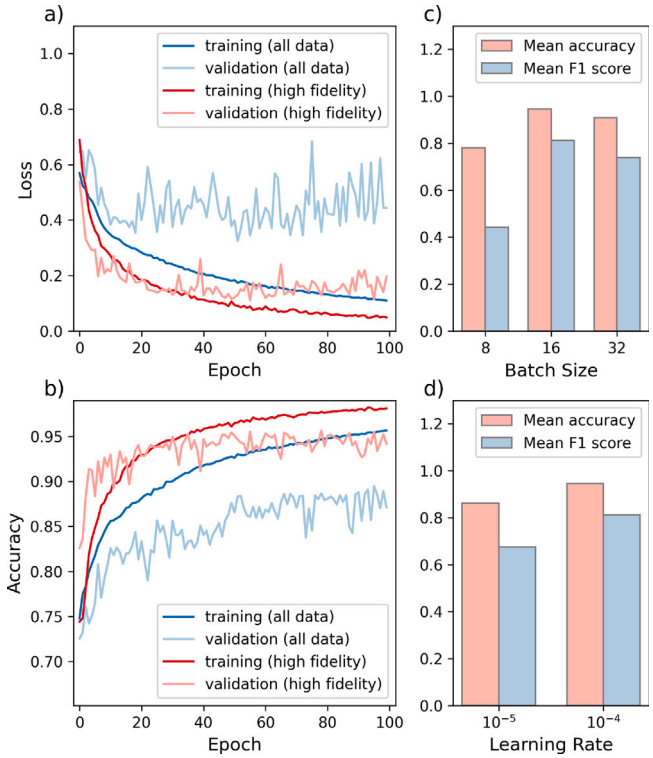

Fig. 5. Effect of data quality, hyperparameter exploration, and training. (a, b) Loss and accuracy vs. epoch. The model trained on the higher quality but smaller data set is more accurate than the one trained on the lower quality but larger data set. (c, d) Mean accuracy and mean F1 score vs. batch size and learning rate. Models trained on either data set were validated using the same images from the high fidelity data set.

3.2. Hyperparameter optimization

We investigated the effect of hyperparameters on the model performance, specifically batch size and learning rate. The metrics used to evaluate the model are the accuracy and the F1 score:

$$\text{Accuracy} = \frac{TP+TN}{TP+TN+FP+FN}, \tag{2}$$

$$\text{F1 Score} = \frac{2TP}{2TP+FP+FN}, \tag{3}$$

where TP is the number of true positives (pixels correctly labeled as "graphene"), TN is the number of true negatives (pixels correctly labeled as "not graphene"), FP is the number of false positives (pixels incorrectly labeled as "graphene"), and FN is the number of false negatives (pixels incorrectly labeled as "not graphene"). Intuitively, accuracy is the percentage of pixels correctly classified. As the harmonic mean of the recall (the proportion of graphene pixels identified as being

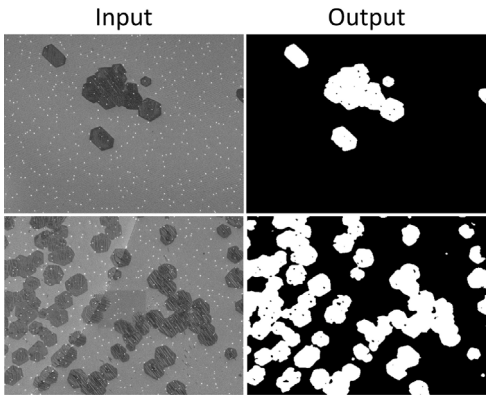

Fig. 6. Performance of trained U-Net model on example images. The model is capable of accurately segmenting the images, which leads to quantitative estimates of coverage. The model also filters most precipitates (seen as white hot spots) in the original images.

graphene pixels) and the precision (ratio of the number of graphene pixels to the number of pixels identified as graphene), the F1 score is a measure of the similarity between the prediction and the ground truth. Fig. 5(c) shows the best values obtained for mean accuracy and mean F1 score when training with a batch size of 8, 16 and 32. Fig. 5(d) shows the best values obtained for mean accuracy and mean F1 score when the initial learning rate was set to 10^{-5} and 10^{-4}. A learning rate of 10^{-3} (not shown) proved to be too high, and the loss diverged. A batch size of 16 and an initial learning rate of 10^{-4} gave the best results. All the models shown in Fig. 5(c, d) were trained on only the high fidelity data.

3.3. Discussion of model performance

Fig. 6 shows the performance of the final model on SEM images of graphene. The model performs well on typical images of graphene, as shown. It is capable of identifying domains of graphene that span across two grains of substrate. It is also capable of ignoring the spots made by precipitates. Both the training and validation losses decrease monotonically with training (Fig. 5(a)), and the difference between them is small — indicating that overfitting was not occurring. The trained model has an accuracy of 0.945 ± 0.089 and an F1 score of 0.812 ± 0.227. We believe that the lower F1 score arose from the selected loss function, which prioritizes accuracy and penalizes incorrect classification of both classes — "graphene" and "not graphene". This was a deliberate selection, since high accuracy is preferable for the purpose of quantifying graphene coverage. We can further see the effect of the loss function in the variance of the accuracy which is very low as compared to that of the F1 score.

Fig. 7 shows the performance of the model on 20 unseen images, for graphene coverage (top panel) and subsequent domain size estimation (lower panel). The images are presented in order of increasing coverage. Overall, the predictions are in good agreement with the actual values across the full range of coverages shown which vary from near zero to around 80%. A possible trend, that low coverages are slightly overestimated and higher coverages are slightly underestimates, emerges from this picture. The lower panel of Fig. 7 compares the actual to predicted domain size for the same twenty images. Overall, the estimated domain size is in good agreement with the true value. As the images selected include both those with low and high coverages, with both small and large domain sizes, accurate prediction of domain size appears possible across diverse types images. This may include, for example, large coverage achieved by a single domain or by numerous smaller domains; alternatively it may include small coverage arising from a single small domain or from disperse miniscule domains spread across the field. Finally, as with the case of coverage described above,

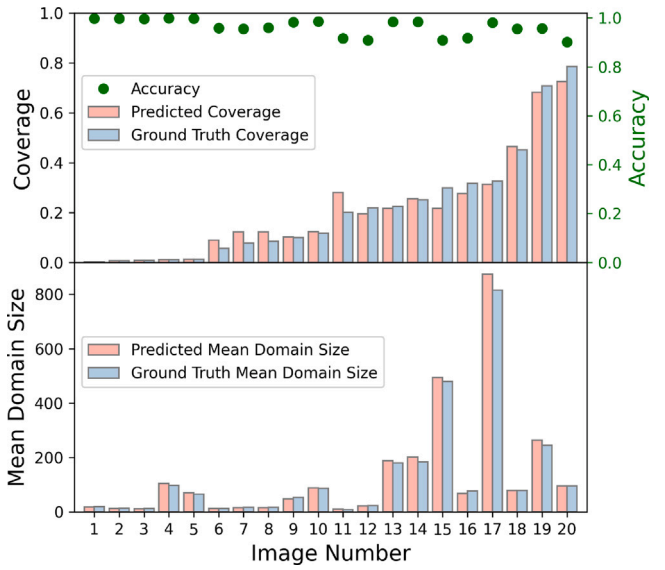

Fig. 7. Performance of the trained model on 20 previously unseen images, in terms of coverage and mean domain size (in pixels). The green dots indicate pixel accuracy, the red and blue bars indicate the predicted and ground truth values. (For interpretation of the references to color in this figure legend, the reader is referred to the web version of this article.)

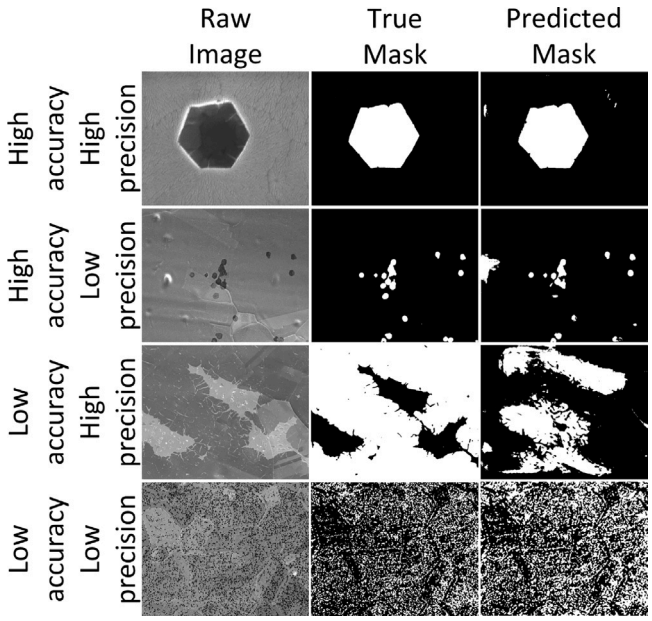

Fig. 8. Examples of SEM images for which the trained U-Net model displays high/low accuracy and high/low precision. The model performs well on images with starker contrast and less complexity. Additionally, spurious artifacts that sometimes appear, such as unwanted precipitates and contaminants, can dramatically affect the results.

while an accurate pixel classification implies accurate predicted domain sizes it is not necessarily the case that an accurate predicted domain size implies accurate pixel classification.

While the model performs well overall, in analyzing its performance we observed that it sometimes generates spurious artifacts in the outputted mask. Fig. 8 shows a few instances that illustrate the disparities we observed in the test results, based on examples corresponding to various combinations of high and low accuracy and precision. In the simplest cases, the model performed with high accuracy and high precision as shown in first row of Fig. 8. The raw image is fairly typical of

SEM images of graphene synthesized by CVD — the graphene domains have a significant difference in contrast with the background, sharp and well-defined boundaries, and there are not many contaminants and/or kinks in the substrate.

The image in the second row shows only a small amount of graphene present. This is an example of an image for which the model showed reasonably high accuracy but low precision. Here, there are a few kinks and bends in the substrate, and some grain boundaries leading to changes in contrast. Here the small proportion of graphene relative to kinks and artifacts in the image causes the neural network to overclassify pixels as "graphene", resulting in a low positive predictive value.

For the image in the third row, the model performs with high precision but low accuracy. This means that pixels classified as graphene are generally indeed graphene, but many actual graphene pixels were not identified as such. The performance here can be attributed to the irregularity and non-hexagonality of the graphene domains, which made the neural network not detect them. We expect that with more illustrative training data, this type of misclassification could be overcome.

The fourth row shows an image that is indicative of the types of SEM micrographs for which the trained model struggled, showing both low precision and low accuracy. The challenging nature of the image arises from the high density of small, distributed nucleation sites and the small domain sizes. Variations in the contrast of the substrate are present, due to the large number of grains, further complicating classification. We expect that these types of images may ultimately prove to be the most challenging ones, as boundaries between graphene and not-graphene occur at high frequency when scanning across pixels, making it difficult for convolution operations to make accurate classification. Additionally, such images are highly sensitive to the pixel-wise accuracy of the training masks.

While these examples highlight some of the challenges encountered by deep learning methods in the classification of SEM micrographs of 2D materials, we expect that several of these challenges could be surmounted as the training data set grows.

3.4. Application of trained U-Net model to other 2D materials

As with graphene, there is interest in rapid segmentation of images of other 2D materials, for example in order to develop better synthesis recipes for transition metal dichalcogenide molybdenum disulfide (MoS_2) [54]. Given the challenges of generating training data and training a neural network for one 2D material, it is of interest to determine whether a neural network trained to segment one 2D material could be used to segment images of other 2D materials as well. If feasible, conversion of a model trained for one material to another could bypass the need for generation of new training data by generalizing the challenge of 2D materials image segmentation. Another option may be transfer learning [55], where a U-Net model trained to segment images of graphene from a large training data set is used as the starting point for a model geared to segment images of other 2D materials by adaption to a smaller data set.

To assess this possibility, Fig. 9 shows the performance of our model (trained on images of graphene) directly applied to several SEM images of 2D MoS_2 [56]. As can be seen from the input images, the domains of MoS_2 are triangular, in contrast to the hexagonal domains of graphene. Otherwise, similar to the graphene images the NN was trained on, these SEM micrographs exhibit no contrast arising from depth. Still, from Fig. 9 we observed that qualitatively the model performs well on the new images, despite not having trained on them. This initial performance is promising for adaptation of the current model to other 2D materials, and indicates the possibility of using transfer learning from our pre-trained model for similar applications to other 2D materials.

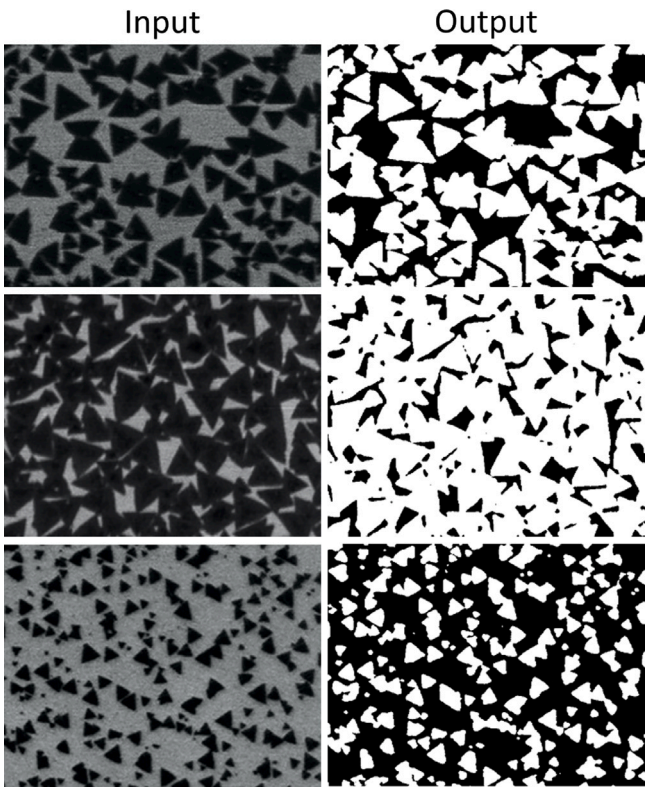

Fig. 9. Performance of U-Net model trained on images of graphene, now directly applied to SEM images of 2D MoS_2. The model performs well, suggesting the possibility of facile transfer learning. Reprinted (adapted) with permission from Jianping Shi, Donglin Ma, Gao-Feng Han, Yu Zhang, Qingqing Ji, Teng Gao, Jingyu Sun, Xiuju Song, Cong Li, Yanshuo Zhang, Xing-You Lang, Yanfeng Zhang, and Zhongfan Liu, ACS Nano 2014 8 (10), 10196–10204. Copyright 2022 American Chemical Society.

3.5. DeepLIFT analysis

While neural networks are sometimes considered to operate as black box methods [57], it can sometimes be useful to analyze the inner workings of the model. We used the DeepLIFT [44] algorithm to analyze the sample image illustrated in Fig. 10(a) to reveal detailed aspects of U-Net classification. DeepLIFT is an approach that determines the relative contributions of different features (pixels of the input image) to the output mask. It then compares this to a reference input, an array of zeros (a black image) to determine the pixels that play a dominant role in determining the likelihood that an output pixel is labeled "graphene" or "not graphene".

Fig. 10(b–d) shows the pixels that are most important for all attributions, graphene attributions, and substrate attributions respectively. It is seen that the edges of the domains are most important in determining what is and what is not graphene. Some pixels in the center of the domains also play a role, to judge the continuity and connectivity of different edges. This observation matches intuition, as edge detection is known to be important for human vision as well [58], and suggests that images that have a greater contrast between graphene and substrate – i.e. sharper edges – might generate better predictions.

4. Conclusion

In this study, we demonstrated the use of a neural network based on the U-Net architecture as an effective approach to the segmentation of SEM images of graphene synthesized by chemical vapor deposition on substrates. Compared to other image segmentation applications, 2D materials segmentation offers new challenges in the form of lack of contrast arising from depth, limited availability of data, and high

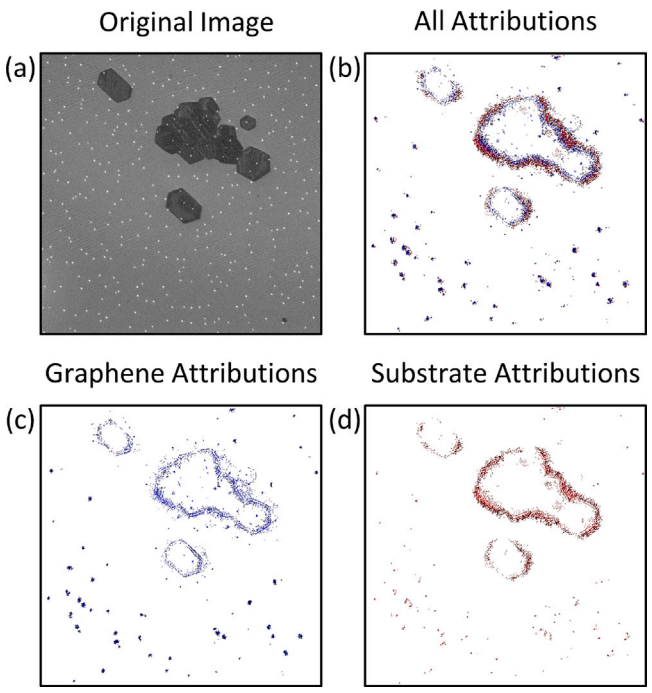

Fig. 10. DeepLIFT analysis of the U-Net classifier, which illustrates the contribution that each input pixel has on the outputted predicted mask. The (a) original image is shown along with (b) all attributions, (c) attributions that contribute to classifying as graphene, and (d) attributions that contribute to classifying as substrate. The pixels that contribute most to classification are those at the edge of the graphene domains.

variance in the size, shape and contrast of domains. The trained model performs with an accuracy of around 90% and an F1 score of around 80%, despite the relatively small sized training data set. Given the accuracy achieved, we expect that model can be used for future high throughput analysis of SEM images for the determination of graphene coverage. We also observed that lesser but high quality training data produces a better model than larger amount of low quality data. Patterns in images for which the trained neural network shows high/low accuracy and precision are identified. We also demonstrated the use of a post processing technique to estimate the graphene domain size using segmented masks which can help compute the effect of annealing and growth recipes on the nucleation density and growth rate, respectively. We expect that automated segmentation of SEM images, in conjunction with associated recipe parameters, will help expedite the optimization of high-quality graphene synthesis. We also highlight the possibility of transfer learning for application to images of other 2D materials.

CRediT authorship contribution statement

Aagam Shah: Conceptualization, Methodology, Software, Validation, Investigation, Data curation, Writing – original draft, Visualization. **Joshua A. Schiller:** Conceptualization, Methodology, Software, Validation, Investigation, Data curation, Writing – original draft, Visualization. **Isiah Ramos:** Validation, Investigation, Data curation. **Darren K. Adams:** Methodology, Software, Data curation. **Sameh Tawfick:** Conceptualization, Methodology, Resources, Writing – review & editing, Supervision, Project administration, Funding acquisition. **Elif Ertekin:** Conceptualization, Methodology, Resources, Writing – review & editing, Supervision, Project administration, Funding acquisition.

Declaration of competing interest

The authors declare that they have no known competing financial interests or personal relationships that could have appeared to influence the work reported in this paper.

Data availability

The raw images and the code can be viewed here: https://github.com/nanoMFG/unet-sem. The trained neural network required to reproduce these findings is available to download at [45].

Acknowledgments

This work was supported by the National Science Foundation (NSF). United States of America through award # 1720701 and # 1922758. This work used the Extreme Science and Engineering Discovery Environment (XSEDE) Bridges-2 at the Pittsburgh Supercomputing Center through allocation ASC190029 and MAT220011.

Appendix A. Supplementary data

Supplementary material related to this article can be found online at https://doi.org/10.1016/j.mtcomm.2023.106127.

References

[1] I. Frank, D.M. Tanenbaum, A.M. van der Zande, P.L. McEuen, Mechanical properties of suspended graphene sheets, J. Vac. Sci. Technol. B 25 (6) (2007) 2558–2561.

[2] D.G. Papageorgiou, I.A. Kinloch, R.J. Young, Mechanical properties of graphene and graphene-based nanocomposites, Prog. Mater. Sci. 90 (2017) 75–127, http://dx.doi.org/10.1016/j.pmatsci.2017.07.004, URL: https://www.sciencedirect.com/science/article/pii/S0079642517300968.

[3] M.-S. Cao, X.-X. Wang, W.-Q. Cao, J. Yuan, Ultrathin graphene: electrical properties and highly efficient electromagnetic interference shielding, J. Mater. Chem. C 3 (26) (2015) 6589–6599.

[4] A. Das, S. Pisana, B. Chakraborty, S. Piscanec, S.K. Saha, U.V. Waghmare, K.S. Novoselov, H.R. Krishnamurthy, A.K. Geim, A.C. Ferrari, et al., Monitoring dopants by Raman scattering in an electrochemically top-gated graphene transistor, Nature Nanotechnol. 3 (4) (2008) 210.

[5] P. Avouris, Graphene: electronic and photonic properties and devices, Nano Lett. 10 (11) (2010) 4285–4294.

[6] Z. Lin, Y. Liu, Y. Yao, O.J. Hildreth, Z. Li, K. Moon, J.C. Agar, C. Wong, Surface engineering of graphene for high performance supercapacitors, in: 2011 IEEE 61st Electronic Components and Technology Conference, ECTC, 2011, pp. 236–241, http://dx.doi.org/10.1109/ECTC.2011.5898519.

[7] M. Kawamoto, P. He, Y. Ito, Green processing of carbon nanomaterials, Adv. Mater. 29 (25) (2017) 1602423.

[8] D. Neumaier, S. Pindl, M.C. Lemme, Integrating graphene into semiconductor fabrication lines, Nature Mater. 18 (6) (2019) 525.

[9] L. Lin, H. Peng, Z. Liu, Synthesis challenges for graphene industry, Nature Mater. 18 (6) (2019) 520–524.

[10] S.H. Choi, S.J. Yun, Y.S. Won, C.S. Oh, S.M. Kim, K.K. Kim, Y.H. Lee, Large-scale synthesis of graphene and other 2D materials towards industrialization, Nature Commun. 13 (1) (2022) 1–5.

[11] J. Li, M. Chen, A. Samad, H. Dong, A. Ray, J. Zhang, X. Jiang, U. Schwingenschlögl, J. Domke, C. Chen, Y. Han, T. Fritz, R.S. Ruoff, B. Tian, X. Zhang, Wafer-scale single-crystal monolayer graphene grown on sapphire substrate, Nature Mater. 21 (2022) 740–747, http://dx.doi.org/10.1038/s41563-021-01174-1, URL: https://www.nature.com/articles/s41563-021-01174-1.

[12] H. Hiura, H. Miyazaki, K. Tsukagoshi, Determination of the number of graphene layers: Discrete distribution of the secondary electron intensity stemming from individual graphene layers, Appl. Phys. Express 3 (2010) 095101, http://dx.doi.org/10.1143/APEX.3.095101/XML, URL: https://iopscience.iop.org/article/10.1143/APEX.3.095101/meta.

[13] B. Han, Y. Lin, Y. Yang, N. Mao, W. Li, H. Wang, K. Yasuda, X. Wang, V. Fatemi, L. Zhou, J.I. Wang, Q. Ma, Y. Cao, D. Rodan-Legrain, Y.Q. Bie, E. Navarro-Moratalla, D. Klein, D. MacNeill, S. Wu, H. Kitadai, X. Ling, P. Jarillo-Herrero, J. Kong, J. Yin, T. Palacios, Deep-learning-enabled fast optical identification and characterization of 2D materials, Adv. Mater. 32 (29) (2020) http://dx.doi.org/10.1002/ADMA.202000953.

[14] S. Masubuchi, E. Watanabe, Y. Seo, S. Okazaki, T. Sasagawa, K. Watanabe, T. Taniguchi, T. Machida, Deep-learning-based image segmentation integrated with optical microscopy for automatically searching for two-dimensional materials, Npj 2D Mater. Appl. 4 (1) (2020) 1–9, http://dx.doi.org/10.1038/s41699-020-0137-z, URL: https://www.nature.com/articles/s41699-020-0137-z, arXiv:1910.12750.

[15] L. Zhu, J. Tang, B. Li, T. Hou, Y. Zhu, J. Zhou, Z. Wang, X. Zhu, Z. Yao, X. Cui, K. Watanabe, T. Taniguchi, Y. Li, Z.V. Han, W. Zhou, Y. Huang, Z. Liu, J.C. Hone, Y. Hao, Artificial neuron networks enabled identification and characterizations of 2D materials and van der waals heterostructures, ACS Nano 16 (2) (2022) 2721–2729, http://dx.doi.org/10.1021/ACSNANO.1C09644/ASSET/IMAGES/MEDIUM/NN1C09644_M003.GIF, URL: https://pubs.acs.org/doi/full/10.1021/acsnano.1c09644.

[16] X. Dong, H. Li, Z. Jiang, T. Grünleitner, I. Güler, J. Dong, K. Wang, M.H. Köhler, M. Jakobi, B.H. Menze, A.K. Yetisen, I.D. Sharp, A.V. Stier, J.J. Finley, A.W. Koch, 3D deep learning enables accurate layer mapping of 2d materials, ACS Nano 15 (2) (2021) 3139–3151, http://dx.doi.org/10.1021/ACSNANO.0C09685/ASSET/IMAGES/MEDIUM/NN0C09685_M011.GIF, URL: https://pubs.acs.org/doi/full/10.1021/acsnano.0c09685.

[17] R.M. Sterbentz, K.L. Haley, J.O. Island, Universal image segmentation for optical identification of 2D materials, Sci. Rep. 11 (1) (2021) 1–8, http://dx.doi.org/10.1038/s41598-021-85159-9, URL: https://www.nature.com/articles/s41598-021-85159-9, arXiv:2103.09449.

[18] Y. He, Y. Ju, Q. Wang, Insights into optical detection and three-dimensional characterization of monolayer molybdenum disulfide thin films based on machine learning, Appl. Surf. Sci. 565 (2021) 150530, http://dx.doi.org/10.1016/J.APSUSC.2021.150530.

[19] Z. Li, J. Lee, F. Yao, H. Sun, Quantifying the CVD-grown two-dimensional materials via image clustering, Nanoscale 13 (36) (2021) 15324–15333, http://dx.doi.org/10.1039/D1NR03802H, URL: https://pubs.rsc.org/en/content/articlelanding/2021/nr/d1nr03802h.

[20] S. Ushiba, N. Miyakawa, N. Ito, A. Shinagawa, T. Nakano, T. Okino, H.K. Sato, Y. Oka, M. Nishio, T. Ono, Y. Kanai, S. Innami, S. Tani, M. Kimuara, K. Matstumoto, Deep-learning-based semantic image segmentation of graphene field-effect transistors, Appl. Phys. Express 14 (3) (2021) 036504, http://dx.doi.org/10.35848/1882-0786/ABE3DB, URL: https://iopscience.iop.org/article/10.35848/1882-0786/abe3db/meta.

[21] B. Yang, M. Wu, W. Teizer, Modified UNet++ with attention gate for graphene identification by optical microscopy, Carbon 195 (2022) 246–252, http://dx.doi.org/10.1016/J.CARBON.2022.03.035.

[22] J. Sanchez-Juarez, M. Granados-Baez, A.A. Aguilar-Lasserre, J. Cardenas, Automated system for the detection of 2D materials using digital image processing and deep learning, Opt. Mater. Express 12 (5) (2022) 1856, http://dx.doi.org/10.1364/ome.454314, URL: https://opg.optica.org/ome/abstract.cfm?URI=ome-12-5-1856.

[23] J.P. Horwath, D.N. Zakharov, R. Mégret, E.A. Stach, Understanding important features of deep learning models for segmentation of high-resolution transmission electron microscopy images, Npj Comput. Mater. 6 (1) (2020) 1–9, http://dx.doi.org/10.1038/s41524-020-00363-x, URL: https://www.nature.com/articles/s41524-020-00363-x.

[24] D. Ciresan, A. Giusti, L. Gambardella, J. Schmidhuber, Deep neural networks segment neuronal membranes in electron microscopy images, in: F. Pereira, C. Burges, L. Bottou, K. Weinberger (Eds.), Advances in Neural Information Processing Systems, 25, Curran Associates, Inc., 2012, URL: https://proceedings.neurips.cc/paper/2012/file/459a4ddcb586f24efd9395aa7662bc7c-Paper.pdf.

[25] A. Aziz Ezzat, M. Bedewy, Machine learning for revealing spatial dependence among nanoparticles: Understanding catalyst film dewetting via gibbs point process models, J. Phys. Chem. C 124 (50) (2020) 27479–27494, http://dx.doi.org/10.1021/acs.jpcc.0c07765, URL: https://doi.org/10.1021/acs.jpcc.0c07765.

[26] K. Faraz, T. Grenier, C. Ducottet, T. Epicier, Deep learning detection of nanoparticles and multiple object tracking of their dynamic evolution during in situ ETEM studies, Sci. Rep. 12 (2022) 1–15, http://dx.doi.org/10.1038/s41598-022-06308-2, URL: https://www.nature.com/articles/s41598-022-06308-2.

[27] R. Jacobs, P. Patki, M.J. Lynch, S. Chen, D. Morgan, K.G. Field, Materials swelling revealed through automated semantic segmentation of cavities in electron microscopy images, Scientific Reports 13 (2023) 5178, http://dx.doi.org/10.1038/s41598-023-32454-2, URL: https://doi.org/10.1038/s41598-023-32454-2.

[28] M. Shen, G. Li, D. Wu, Y. Liu, J.R. Greaves, W. Hao, N.J. Krakauer, L. Krudy, J. Perez, V. Sreenivasan, B. Sanchez, O. Torres-Velázquez, W. Li, K.G. Field, D. Morgan, Multi defect detection and analysis of electron microscopy images with deep learning, Comput. Mater. Sci. 199 (2021) 110576, http://dx.doi.org/10.1016/j.commatsci.2021.110576, URL: https://www.sciencedirect.com/science/article/pii/S0927025621003037.

[29] R. Jacobs, M. Shen, Y. Liu, W. Hao, X. Li, R. He, J.R. Greaves, D. Wang, Z. Xie, Z. Huang, C. Wang, K.G. Field, D. Morgan, Performance and limitations of deep learning semantic segmentation of multiple defects in transmission electron micrographs, Cell Rep. Phys. Sci. 3 (5) (2022) 100876, http://dx.doi.org/10.1016/j.xcrp.2022.100876, URL: https://www.sciencedirect.com/science/article/pii/S2666386422001503.

[30] R. Jacobs, Deep learning object detection in materials science: Current state and future directions, Comput. Mater. Sci. 211 (2022) 111527, http://dx.doi.org/10.1016/j.commatsci.2022.111527, URL: https://www.sciencedirect.com/science/article/pii/S0927025622002804.

[31] J. Bals, M. Epple, Deep learning for automated size and shape analysis of nanoparticles in scanning electron microscopy, RSC Adv. 13 (2023) 2795–2802, http://dx.doi.org/10.1039/D2RA07812K.

[32] G. Kavuran, SEM-Net: Deep features selections with binary particle swarm optimization method for classification of scanning electron microscope images, Mater. Today Commun. 27 (2021) 102198, http://dx.doi.org/10.1016/J.MTCOMM.2021.102198.

[33] M.H. Modarres, R. Aversa, S. Cozzini, R. Ciancio, A. Leto, G.P. Brandino, Neural network for nanoscience scanning electron microscope image recognition, Sci. Rep. 7 (1) (2017) 1–12, http://dx.doi.org/10.1038/s41598-017-13565-z, URL: https://www.nature.com/articles/s41598-017-13565-z.

[34] A. Krizhevsky, I. Sutskever, G.E. Hinton, ImageNet classification with deep convolutional neural networks, in: F. Pereira, C. Burges, L. Bottou, K. Weinberger (Eds.), Advances in Neural Information Processing Systems, Vol. 25, Curran Associates, Inc., 2012, URL: https://proceedings.neurips.cc/paper_files/paper/2012/file/c399862d3b9d6b76c8436e924a68c45b-Paper.pdf.

[35] K. He, X. Zhang, S. Ren, J. Sun, Deep residual learning for image recognition, in: 2016 IEEE Conference on Computer Vision and Pattern Recognition, CVPR, 2016, pp. 770–778, http://dx.doi.org/10.1109/CVPR.2016.90.

[36] O. Ronneberger, P. Fischer, T. Brox, U-net: Convolutional networks for biomedical image segmentation, in: International Conference on Medical Image Computing and Computer-Assisted Intervention, Springer, 2015, pp. 234–241.

[37] O. Oktay, J. Schlemper, L.L. Folgoc, M. Lee, M. Heinrich, K. Misawa, K. Mori, S. McDonagh, N.Y. Hammerla, B. Kainz, et al., Attention u-net: Learning where to look for the pancreas, 2018, arXiv preprint arXiv:1804.03999.

[38] H. Dong, G. Yang, F. Liu, Y. Mo, Y. Guo, Automatic brain tumor detection and segmentation using U-net based fully convolutional networks, in: Annual Conference on Medical Image Understanding and Analysis, Springer, 2017, pp. 506–517.

[39] T. Falk, D. Mai, R. Bensch, Ö. Çiçek, A. Abdulkadir, Y. Marrakchi, A. Böhm, J. Deubner, Z. Jäckel, K. Seiwald, et al., U-net: deep learning for cell counting, detection, and morphometry, Nature Methods 16 (1) (2019) 67.

[40] C. Cao, F. Liu, H. Tan, D. Song, W. Shu, W. Li, Y. Zhou, X. Bo, Z. Xie, Deep learning and its applications in biomedicine, Genom. Proteom. Bioinform. 16 (1) (2018) 17–32, http://dx.doi.org/10.1016/j.gpb.2017.07.003, URL: https://www.sciencedirect.com/science/article/pii/S1672022918300020.

[41] R.B. Oliveira, E. Mercedes Filho, Z. Ma, J.P. Papa, A.S. Pereira, J.M.R. Tavares, Computational methods for the image segmentation of pigmented skin lesions: a review, Comput. Methods Programs Biomed. 131 (2016) 127–141.

[42] J. MacQueen, et al., Some methods for classification and analysis of multivariate observations, in: Proceedings of the Fifth Berkeley Symposium on Mathematical Statistics and Probability, Vol. 1, No. 14, Oakland, CA, USA, 1967, pp. 281–297.

[43] J.A. Schiller, R. Toro, A. Shah, M. Surana, K. Zhang, M. Robertson, K. Miller, K. Cruse, K. Liu, B. Seong, C. Seol, I.T. Foster, B.J. Blaiszik, B. Galewsky, D. Adams, D.S. Katz, P. Ferreira, E. Ertekin, S. Tawfick, Crowd-sourced data and analysis tools for advancing the chemical vapor deposition of graphene: Implications for manufacturing, ACS Appl. Nano Mater. 3 (10) (2020) 10144–10155, http://dx.doi.org/10.1021/acsanm.0c02018.

[44] A. Shrikumar, P. Greenside, A. Kundaje, Learning important features through propagating activation differences, in: Proceedings of the 34th International Conference on Machine Learning-Volume 70, JMLR.org, 2017, pp. 3145–3153.

[45] A. Shah, J.A. Schiller, I. Ramos, S. Tawfick, E. Ertekin, CVD graphene SEM image segmentation, 2022, http://dx.doi.org/10.5281/zenodo.7063245.

[46] E.G. de Mariscal, C.G.-L. de Haro, W. Ouyang, L. Donati, E. Lundberg, M. Unser, A. Mu noz-Barrutia, D. Sage, DeepImageJ: A user-friendly environment to run deep learning models in ImageJ, Nature Methods 18 (2021) 1192–1195, http://dx.doi.org/10.1038/s41592-021-01262-9, URL: https://www.nature.com/articles/s41592-021-01262-9.

[47] R. Brunelli, Template Matching Techniques in Computer Vision : Theory and Practice, Wiley, 2009, p. 338.

[48] J.A. Schiller, M.G. Robertson, K.M. Miller, K.J. Cruse, K. Liu, D.K. Adams, B. Galewsky, E. Ertekin, S.H. Tawfick, SEM image processing tool, 2018, http://dx.doi.org/10.21981/8W7X-7V98, URL: https://nanohub.org/resources/gsaimage.

[49] R. Aversa, M.H. Modarres, S. Cozzini, R. Ciancio, NFFA-EUROPE - SEM dataset, 2018, http://dx.doi.org/10.23728/B2SHARE.19CC2AFD23E34B92B36A1DFD0113A89F, Dataset of 18 577 SEM images produced at CNR-IOM (Trieste) not for any other scientific scope related to their content. This work has been done within the NFFA–EUROPE project (www.nffa.eu) and has received funding from the European Union's Horizon 2020 Research and Innovation Programme under grant agreement No. 654360 NFFA URL: https://b2share.eudat.eu/records/19cc2afd23e34b92b36a1dfd0113a89f.

[50] F. Chollet, et al., Keras, 2015, https://keras.io.

[51] M. Abadi, A. Agarwal, P. Barham, E. Brevdo, Z. Chen, C. Citro, G.S. Corrado, A. Davis, J. Dean, M. Devin, S. Ghemawat, I. Goodfellow, A. Harp, G. Irving, M. Isard, Y. Jia, R. Jozefowicz, L. Kaiser, M. Kudlur, J. Levenberg, D. Mané, R. Monga, S. Moore, D. Murray, C. Olah, M. Schuster, J. Shlens, B. Steiner, I. Sutskever, K. Talwar, P. Tucker, V. Vanhoucke, V. Vasudevan, F. Viégas, O.

Vinyals, P. Warden, M. Wattenberg, M. Wicke, Y. Yu, X. Zheng, TensorFlow: Large-scale machine learning on heterogeneous systems, 2015, URL: https://www.tensorflow.org/, Software available from tensorflow.org.

[52] J. Canny, A computational approach to edge detection, IEEE Trans. Pattern Anal. Mach. Intell. PAMI-8 (6) (1986) 679–698, http://dx.doi.org/10.1109/TPAMI.1986.4767851.

[53] J. Matas, C. Galambos, J. Kittler, Progressive probabilistic hough transform, in: British Machine Vision Conference, 1998.

[54] A. Gupta, T. Sakthivel, S. Seal, Recent development in 2D materials beyond graphene, Prog. Mater. Sci. 73 (2015) 44–126, http://dx.doi.org/10.1016/J.PMATSCI.2015.02.002.

[55] K. Weiss, T.M. Khoshgoftaar, D. Wang, A survey of transfer learning, J. Big Data 3 (1) (2016) http://dx.doi.org/10.1186/s40537-016-0043-6.

[56] J. Shi, D. Ma, G.F. Han, Y. Zhang, Q. Ji, T. Gao, J. Sun, X. Song, C. Li, Y. Zhang, X.Y. Lang, Y. Zhang, Z. Liu, Controllable growth and transfer of monolayer MoS2 on au foils and its potential application in hydrogen evolution reaction, ACS Nano 8 (10) (2014) 10196–10204, http://dx.doi.org/10.1021/NN503211T/SUPPL_FILE/NN503211T_SI_001.PDF, URL: https://pubs.acs.org/doi/full/10.1021/nn503211t.

[57] J.E. Dayhoff, J.M. DeLeo, Artificial neural networks, Cancer 91 (S8) (2001) 1615–1635, http://dx.doi.org/10.1002/1097-0142(20010415)91:8+<1615::AID-CNCR1175>3.0.CO;2-L, URL: https://acsjournals.onlinelibrary.wiley.com/doi/abs/10.1002/1097-0142%2820010415%2991%3A8%2B%3C1615%3A%3AAID-CNCR1175%3E3.0.CO%3B2-L.

[58] D. Marr, E. Hildreth, Theory of edge detection, Proc. R. Soc. Lond. Ser. B. Biol. Sci. 207 (1167) (1980) 187–217.